NANO · MICRO small
www.small-journal.com

Self-Assembled Construction of Robust and Super Elastic Graphene Aerogel for High-Efficient Formaldehyde Removal and Multifunctional Application

*Wuyou Wang, Xiaowen Zhao, and Lin Ye**

Simultaneously achieving exceptional mechanical strength and resilience of graphene aerogel (GA) remains a challenge, while GA is an ideal candidate for formaldehyde removal. Herein, flexible polyethyleneimine (PEI) is grafted chemically onto carbon nanotube (CNT) surface, and CNT-PEI@reduced GA (rGA) is fabricated via hydrothermal self-assembly, pre-frozen, and hydrazine reduction process. Introducing CNT-PEI contributes to well-interconnected/robust 3D network construction by connecting reduced graphene oxide (rGO) nanosheets through enhancing cross-linking, while entangled CNT-PEI is intercalated into rGO layers to avoid serious restacking of sheets, producing larger surface area and more formaldehyde adsorption sites. Ultralight CNT-PEI@rGA exhibits extreme high strength (276.37 kPa), reversible compressibility at 90% strain, and structural stability, while FA adsorption capacity reached 568.41 mg g^{-1}, ≈3.28 times of rGA, derivable from synergistic chemical-physical adsorption effect. Furthermore, CNT-PEI@rGA is ground into powder for first preparing polyoxymethylene (POM)/CNT-PEI@rGA composite, while formaldehyde emission amount is 69.63%/73.96% lower than that of POM at 60/230 °C. Moreover, CNT-PEI@rGA presents outstanding piezoresistive-sensing and thermal insulation properties, exhibiting high strain sensitivity, wide strain detection range, and long-term durability.

1. Introduction

Graphene aerogel (GA), owing to unique 3D microstructure, ultralight weight, high porosity/specific surface area, chemical/thermal stability, etc., has drawn considerable attention in various fields of energy storage,[1–2] flexible electronic devices,[3,4] environmental remediation,[5,6] and so on. By using graphene oxide (GO) as precursors, self-assembly method combined with freeze-drying is regarded as a promising green approach involving simple process and convenient operation. However, the mechanical defects of GA arise from weak connection (π-π stacking and Van der Waals' force) among graphene nanosheets in the assembly process, resulting in structure collapse and deformation when undergoing external force, which makes GA unable to satisfy different requirements in practical scenes.

Up to date, some additives have been introduced to tackle above issue by exerting strong interactions among constituents and effective intercalation between graphene layers, e.g., sodium borate,[7] cellulose,[8] polyvinyl alcohol,[9] carbon nanofiber,[10] etc. Among them, due to its excellent mechanical properties, high conductivity, and large aspect ratio, carbon nanotube (CNT) is considered as a promising building block for GA. A combination of 1D CNT with 2D graphene can hopefully pave the way for fabricating multifunctional 3D GA with superior mechanical properties, and thereby some studies have been recently dedicated to graphene/CNT aerogels. For example, Peng Lv et al.[11] prepared graphene/CNT composite aerogel by hydrothermal method with maximum compressive strain of 80% as thermal interface materials. Yan Qin et al.[12] prepared GA reinforced by modifying CNT with metal ions for microwave absorption, which exhibited compressibility at the strain up to 95%, but mechanical strength was only ≈18 KPa. Jannatul Dil Afroze et al.[13] fabricated hierarchical honeycomb graphene/CNT aerogels with multifunctional mechanical and electrical properties with compressive strength of 73.9 KPa at 50% strain. Despite several progresses, the bottleneck and challenge remain simultaneous achievement of exceptional mechanical strength and resilience of graphene/CNT aerogel without deteriorating its low density and good conductivity. Moreover, low water-soluble CNT is easy to aggregate and disperses poorly in GA, resulting in unsatisfactory mechanical improvement of composite aerogels.

Formaldehyde (FA) is a typical carcinogenic volatile organic compound (VOC) and widely applied to manufacture various industrial products, such as cosmetics, resins/plastics, textiles, and so on. Especially for polyoxymethylene (POM), as a common engineering plastic in construction, machinery parts, automobiles, etc., it releases residual free FA during long-term use and depolymerization under heat and oxygen in high-temperature melting process, which is harmful to human health and environment. Impressively, FA molecule adsorption on graphene has been reported theoretically and experimentally,[14,15] and predictably, GA with high specific surface

---

W. Wang, X. Zhao, L. Ye
State Key Laboratory of Polymer Materials Engineering
Polymer Research Institute of Sichuan University
Chengdu 610065, P. R. China
E-mail: sklpme@scu.edu.cn

The ORCID identification number(s) for the author(s) of this article can be found under https://doi.org/10.1002/smll.202300234.

DOI: 10.1002/smll.202300234

area and pore volume is also expected as an ideal candidate in field of FA removal. Nevertheless, FA adsorption capacity of neat GA is less than expectations due to stacking of graphene nanosheets, while relevant modified studies are limitedly published in recent years. For instance, Jie Ma[16] et al. manufactured composite GAs by direct additions of CNT into GO solution with 18 mg g^{-1} FA adsorption capacity. Lirui Wu [17] et al. prepared ethylenediamine- modified graphene sponge with enhanced FA adsorption capacity of 22.8 mg g^{-1}, and amine groups of ethylenediamine was essential for improvement of FA removal. Wenkun Zhang [18] et al. fabricated chitosan-modified metal organic framework/Tetraethylene pentamine-functionalized GA aerogel and its FA adsorption capacity increased to ≈197.89 mg g^{-1}. Unfortunately, FA removal performances of these reported adsorbents are still dissatisfied, while more importantly, poor structural stability of aerogels restrict its practical applications. Besides, almost no literature was available on decreasing formaldehyde emission of POM to achieve low VOC product by incorporation of GA, as far as we know.

In this work, polyethyleneimine (PEI), as a flexible polymer with water-solubility and high amine density, is selected as an assistant reduction agent and crosslinker for construction of GA due to high affinity between amine groups and oxygen functional groups among constituents. Moreover, abundant amine groups can provide active sites for reactions with formaldehyde. Therefore, PEI was first grafted chemically onto CNT surface (CNT-PEI) to increase aqueous dispersion of CNT for further reaction. Subsequently, CNT-PEI@reduced GA (rGA) was fabricated via hydrothermal assembly, pre-frozen and hydrazine vapor reduction process by using GO and CNT-PEI as precursors. Such unique 1D/2D assembly strategy provided several merits for CNT-PEI@rGA: First, well-interconnected and robust 3D network framework was constructed through strong interfacial interaction between reduced graphene oxide (rGO) and CNT-PEI, which endowed CNT-PEI@rGA with ultralow density, high strength, and super-elasticity simultaneously due to support and crosslinking effect of CNT-PEI. Second, the restacking of nanosheets was inhibited by effective intercalation of CNT-PEI between rGO layers to increase specific surface area and expose more reactive sites, predictably endowing CNT-PEI@rGA with remarkable FA removal capability. Meanwhile, POM/CNT-PEI@rGA composite was further prepared via conventional melt-processing for the first time and its formaldehyde emission amount (FEA) was expected to be reduced greatly. Third, CNT-PEI@rGA showed excellent conductivity, piezoresistive-sensing, and thermal insulation properties, etc., exhibiting significant application potentials in environmental remediation, smart electronic devices, heat insulating fields, etc.

2. Results and Discussion

2.1. Fabrication and Structure Characterization of CNT-PEI@rGA

The fabricating procedure of CNT-PEI@rGA was shown in **Figure 1**, mainly including mixing, hydrothermal assembly, pre-frozen, and hydrazine vapor reduction process. First, CNT-PEI was prepared as a building block of composite aerogel, while FTIR, TGA, and TEM analysis confirmed the covalent functionalization of CNT with PEI grafting ratio of 29.34% and morphology of thickening tubular CNT covered with PEI (Figure S1(a–d), Supporting Information and **Figure 2**a). Afterward, GO and CNT-PEI were adequately mixed and sonicated in DI water to form a well-dispersed suspension, and CNT-PEI exhibited outstanding water-solubility and dispersion stability owing to hydrophilic amine groups (Figure S1(d), Supporting Information). Then, the mixture was hydrothermally treated to obtain CNT-PEI@rGO hydrogel. Herein, PEI simultaneously served as an assistant reduction agent and crosslinker, while CNT inhibited the restacking of rGO nanosheets by acting as a spacer during the self-assembly between GO and CNT-PEI. Next, the hydrogel components were repelled from the solidification front and accumulated as "cell walls" between the growing ice crystals during pre-frozen, and then aerogel was formed by their subliming in the freeze-drying process. Subsequently, it was reduced by moderate hydrazine vapor

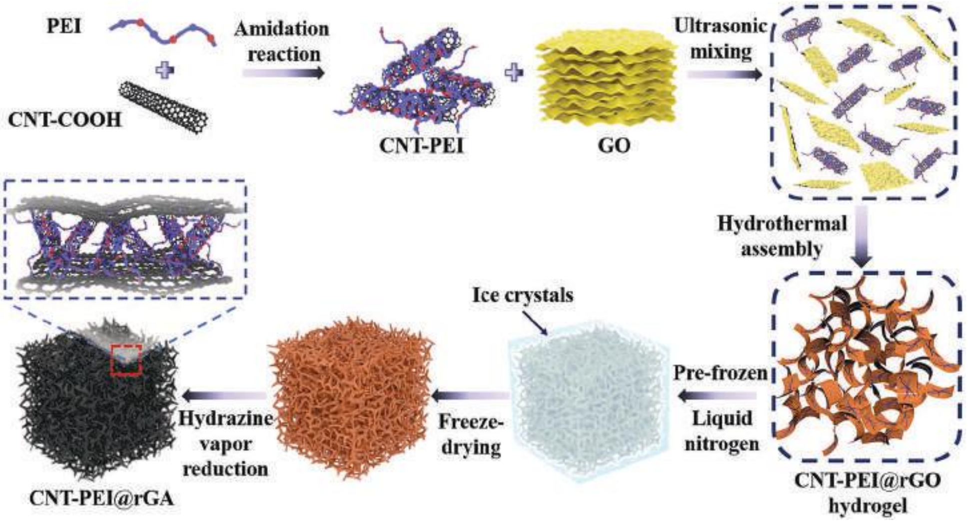

Figure 1. Scheme of fabricating procedure of CNT-PEI@rGA.

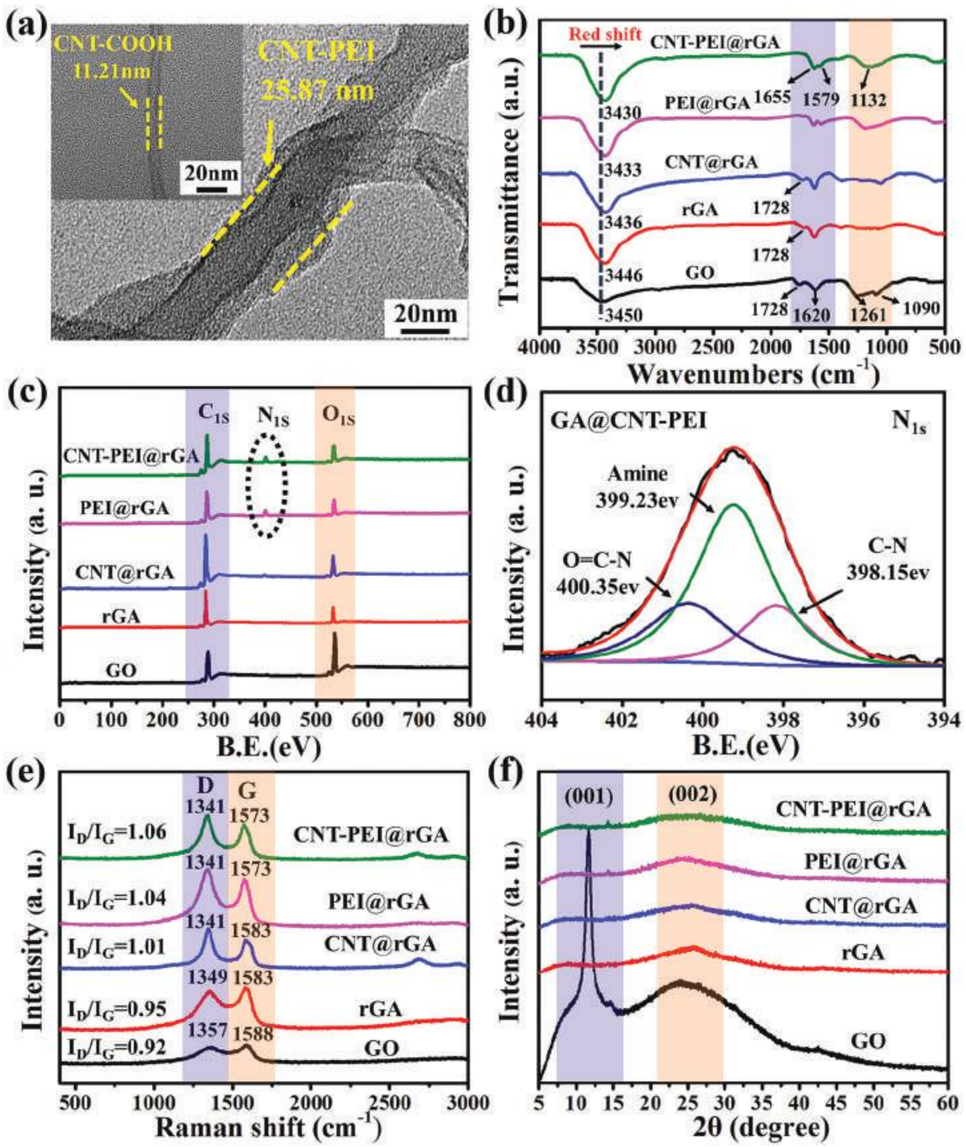

Figure 2. a) TEM images of CNT-COOH (inset) and CNT-PEI, b) FTIR spectra, c) XPS full spectrum, d) N_{1S} spectra of CNT-PEI@rGA, e) Raman spectra, and f) XRD patterns of GO, rGA, CNT@rGA, PEI@rGA, and CNT-PEI@rGA samples.

treatment to remove residual oxygen-containing groups, and thus CNT-PEI@rGA was obtained finally.

The surface functional groups of aerogel samples were identified by FT-IR in Figure 2b. The characteristic peaks of GO appeared at 1090 cm^{-1} (O–H stretching vibration), 1261 cm^{-1} (C–O–C stretching vibration),1620 cm^{-1} (C=C ring vibration), 1728 cm^{-1} (C=O stretching vibration of carboxyl groups) and 3450 cm^{-1} (O–H stretching vibration), respectively. Compared with GO, peaks at 1728 and 1261 cm^{-1} were merely weakened to a certain extent for rGA and CNT@rGA, indicating some carboxyl and epoxy groups were still reserved in the hydrothermal and hydrazine vapor reduction process, while O–H stretching vibration peak was slightly shifted from 3450 to 3436 cm^{-1} for CNT@rGA, resulting from enhanced hydrogen bonding owing to introduction of CNT-COOH. By comparison, for PEI@rGA and CNT-PEI@rGA, the bands corresponded to oxygen-containing groups almost disappeared, suggesting reduction was enhanced significantly due to incorporation of PEI or CNT-PEI, while new peaks at 1655, 1579, and 1132 cm^{-1} were assigned to C=O stretching vibration in amide I band or C=C skeletal vibration, N–H bending vibration in amide II band, and C–N stretching vibration, respectively, indicating formation of covalent bonds among constituents through amidation and nucleophilic substitution reaction between oxygen-containing and amine groups in aerogel systems. Moreover, for these two samples, apparent red-shift of O–H stretching vibration peak was observed in comparison with samples in absence of PEI, ascribed to strong hydrogen bonding between GO and PEI.

XPS was employed to analyze element composition of aerogel samples (Figure 2c-d and Table S1, Supporting Information). In Figure 2c, two prominent peaks at 286.85 eV (C_{1s}) and 533.26 eV

(O_{1s}) were detected for all samples, while only for PEI@rGA and CNT-PEI@rGA, new signal of N_{1s} appeared at 401.25 eV and the content of N element reached 7.18% and 6.98%, respectively. Additionally, compared to GO, the content of O element was much lower due to efficient reduction progress for aerogel samples. Furthermore, N_{1s} spectrum of CNT-PEI@rGA was deconvoluted into three peaks in Figure 2d: 400.35 eV (O=C–N), 399.23 eV (Amine), and 398.15 eV (C–N), further demonstrating CNT-PEI were covalently linked to the GO surface by amidation and nucleophilic substitution reaction.

The Raman spectra of aerogel samples were illustrated in Figure 2e, and intensity ratio (I_D/I_G) were used to quantitatively evaluate the disorder degree of samples. It was seen that all samples exhibited two characteristic peaks, i.e., D peak (1341-1357 cm^{-1}), and G peak (1573–1588 cm^{-1}), while two peaks of aerogel samples shifted to lower wavenumber in comparison with GO. Compared to GO (0.92), I_D/I_G value increased at different degree for aerogel samples. Especially, the I_D/I_G value of PEI@rGA was higher than that of CNT@rGA, indicating that intercalation of PEI with long molecular chains into rGO layers destroyed its regularity more remarkably that that of CNT, and thus intercalation of CNT-PEI into rGO layers led to the relatively higher disorder degree and further increase of the I_D/I_G value. Moreover, owing to reduction effect of PEI, numerous newly-formed sp^2 domains with small size reduced the average size of sp^2 domains of rGO, also resulting in an increase of the I_D/I_G value, as demonstrated by Stankovich et al.[19]

Figure 2f depicted further the XRD patterns of aerogel samples, and unlike the sharp (001) diffraction peak of GO at 11.8° (d-spacing = 0.75 nm), aerogel samples presented a broad peak ≈23.5° (d-spacing = 0.39 nm) corresponding to (002) crystal plane of rGO, resulting from the removal of oxygen-rich groups and partial restoration of graphite structure by reduction. Furthermore, compared with rGA, the (002) band of PEI@rGA and CNT@rGA showed slight shift towards lower 2θ value and broadened, while for CNT-PEI@rGA, the peak became broader and even almost disappeared, indicating that restacking of rGO nanosheets was effectively inhibited by introduction of CNT-PEI.

2.2. Well-Interconnected 3D Network Structure and Mechanical Properties of CNT-PEI@rGA

The average densities of as-prepared aerogels were in rang of 6.2–9.6 mg cm^{-3} (Figure S2(a), Supporting Information), which belonged to the ultralight materials ($\rho < 10$ mg cm^{-3}), and more vividly, ultralight CNT-PEI@rGA was rested atop a flower without causing any deformation in **Figure 3**a. SEM and TEM images showed the morphologies of aerogel samples. For rGA (Figure S2(b), Supporting Information), most crinkly rGO nanosheets were overlapped randomly and stacked seriously without connection to each other. In contrast, PEI@rGA exhibited interconnected porous network and bridging structure were found in Figure S2(c), Supporting Information, while for CNT@rGA, almost no catastrophic stacking phenomenon of rGO sheets was observed in Figure S2(d) (Supporting Information). As shown in Figure 3b-c, CNT-PEI@rGA presented more regular and well-interconnected 3D network framework, with pore sizes ranging from ≈10 µm to 50 µm. Moreover, detailed observations for CNT-PEI@rGA further proclaimed interconnections between rGO and CNT-PEI: CNT-PEI covered on walls and wall-to-wall junctions of rGO sheets (Figure 3d), and intercalated between the rGO sheets (Figure 3e). Additionally, SEM images showed that entangled CNT-PEI was homogeneously distributed on rGO sheets for CNT-PEI@rGA, while some agglomeration of CNT was observed for CNT@rGA in Figure S2(e–f) (Supporting Information). Besides, EDS spectra of CNT-PEI@rGA exhibited uniform distribution of C, O, and N elements with the content of 77.04, 15.12, and 7.84 wt.% in Figure 3f, respectively. Furthermore, TEM images confirmed that tubular CNT-PEI were well-embedded and uniformly adhered to rGO substrates (Figure 3g). Figure 3h showed that light cyclic patterns and multi-sets of hexagonal spots were both detected in SAED, ascribed possibly to the presence of CNT-PEI and multi-layer rGO sheets, respectively.[20] Therefore, introduction of CNT-PEI played a positive role in 3D network framework construction of aerogel because rGO nanosheets were connected to each other through enhanced cross-linking effect of CNT-PEI, and CNT-PEI was intercalated into rGO layers to avoid serious restacking in the meantime.

Nitrogen sorption isotherms of aerogel samples were evaluated using BET and BJH methods, and the obtained pore properties were summarized in **Table 1**. As shown in Figure S3 (Supporting Information), typical Type IV isotherms of all samples suggested the presence of abundant mesopores, and pore size distribution curves illustrated that pore diameter ranged in 2–100 nm approximately for all samples. From Table 1, the value of BET specific surface area and total pore volumes increased in the order of rGA < PEI@rGA < CNT@rGA < CNT-PEI@rGA, and especially these value of CNT-PEI@rGA reached 364.24 m^2 g^{-1} and 1.75 cm^3 g^{-1}, which were 1.74 and 7.18 times larger than those of rGA, respectively. The results demonstrated incorporation of CNT-PEI produced more mesopores and larger specific surface area owing to effective intercalation effect served as interlayer spacers.

CNT-PEI@rGA was ultralight and low-density, yet it was robust and supported 100 g weight (more than 2000 times of its own weight) without noticeable deformation in Figure S4(a) (Supporting Information). As showed in **Figure 4**a and Movie S1 (Supporting Information), cylinder-shaped CNT-PEI@rGA was capable of bearing compression at 90% strain and recovered to original shape rapidly without cracking or collapsing when loading was released. A series of compression tests were used to evaluate mechanical properties of aerogel samples with similar initial density. The compression curves of all specimens at 90% strains (ε) were showed in Figure 4b, and it was observed that they exhibited similar trends: a linear-elastic region at $\varepsilon < 10\%$, a yield region at $10\% < \varepsilon < 60\%$, and a densification region at $\varepsilon > 60\%$, assigned to elastic-bending, buckling, and overlapping of cell walls, respectively. Furthermore, Figure 4c summarized compressive stress and Young's modulus of all samples upon 90% strain. Compared with rGA (11.96 kPa, 0.07 MPa), stress and Young's modulus of CNT@rGA and PEI@rGA increased, while those values of CNT-PEI@rGA further increased to 276.37 kPa and 1.52 MPa, ≈22.1 and 20.7 times higher than those of rGA, respectively, indicating remarkable mechanical reinforcement of CNT-PEI@rGA. Moreover, successive loading-unloading tests were performed for all samples under various strains of

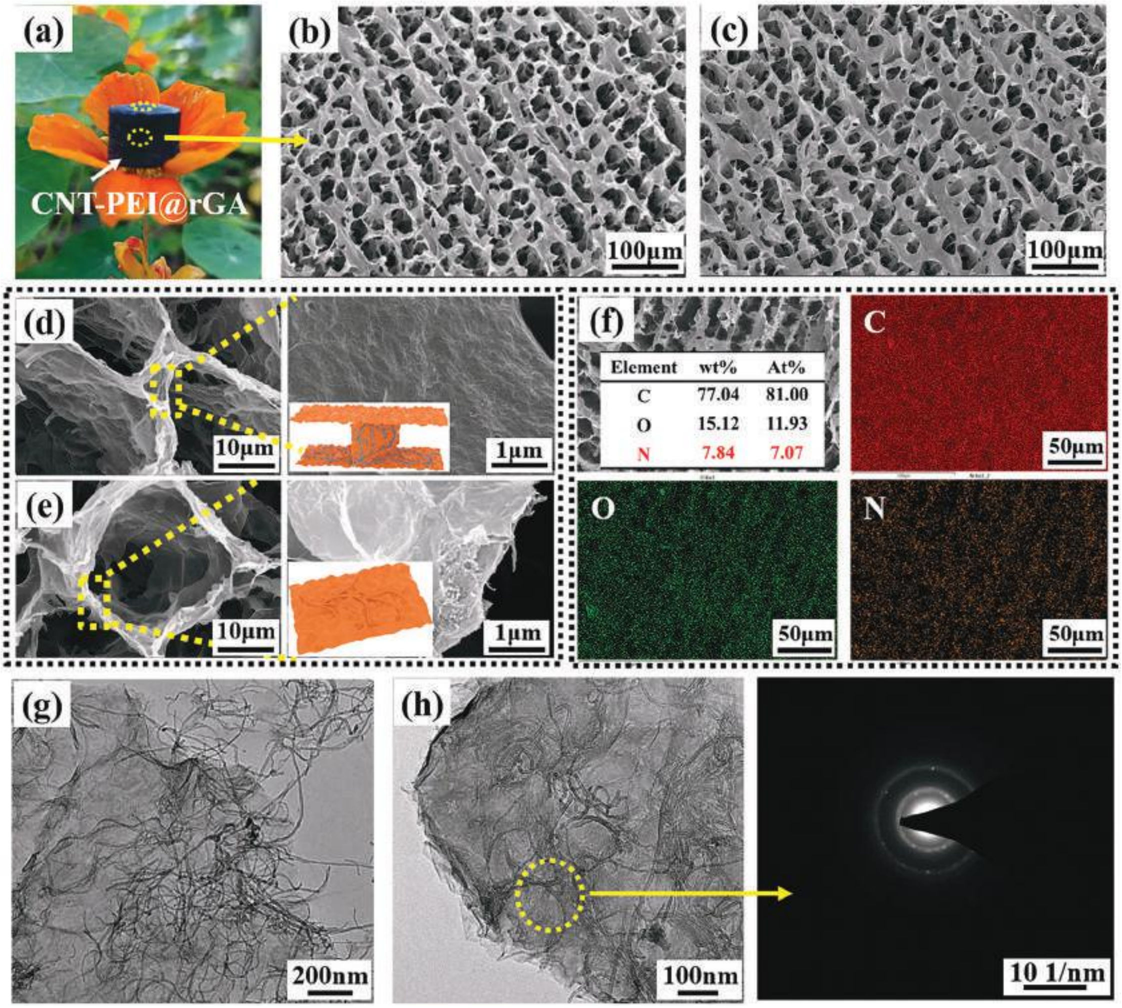

Element	wt%	At%
C	77.04	81.00
O	15.12	11.93
N	7.84	7.07

Figure 3. a) Digital photograph of ultralight CNT-PEI@rGA standing on top of a flower. b,c) SEM images of CNT-PEI@rGA in b) top view and c) side view with low magnification. d,e) SEM images of CNT-PEI@rGA with high magnification, and cartoon models (insets) related to interconnections between rGO and CNT-PEI. f) EDS mapping images of CNT-PEI@rGA. g,h) TEM images of CNT-PEI@rGA with various magnification, and SAED patterns at the labeled area.

30%, 60% and 90% in Figure S4(b–f) (Supporting Information). Notably, rGA was deformed permanently in a macroscopic configuration after successive compression, while SEM images showed its structural collapse in micro-scale (Figure S4(b–c), Supporting Information). For CNT@rGA and PEI@rGA, their resilience was improved due to introduction of CNT-COOH and PEI (Figure S4(d–e), Supporting Information). As for CNT-PEI@rGA, compressive stress remained above zero until $\varepsilon = 0$ during the unloading process at each strain and its original macroscopic size was completely recoverable in Figure S4(f) (Supporting Information), demonstrating excellent reversible compressibility of CNT-PEI@rGA. Additionally, CNT-PEI@rGA was further subjected to cyclic compression experiment (100 cycles) at a set strain of 80% in Figure 4d, while compressive stress, Young's modulus and energy loss coefficient varying with cycles were shown in Figure 4e. It was found that hysteresis loops were slightly shrunk with the increasing number of cycles and well-interconnected 3D network structure was perfectly maintained after 100 cycles by SEM observation in the inset of Figure 4d. As depicted in Figure 4e, compressive stress, Young's modulus, and energy loss coefficient values of 100th cycles were 53.22 kPa, 364.09 kPa, and 0.62, corresponding to retention ratio of 95.65%, 95.79% and 91.72%, respectively, which confirmed outstanding structural stability and durability of CNT-PEI@rGA. According to Table S2 (Supporting Information) and Figure 4f,[11,21–30] CNT-PEI@rGA exhibited better mechanical properties that exceeded most reported elastic GAs ($\varepsilon > 80\%$),

Table 1. Pore properties of rGA, CNT@rGA, PEI@rGA, and CNT-PEI@rGA samples.

Samples	BET specific surface area [m^2 g^{-1}]	BJH total pore volumes [cm^3 g^{-1}]	BJH pore diameter [nm]
rGA	132.82	0.21	3.41
PEI@rGA	215.41	0.69	3.81
CNT@rGA	318.52	0.98	3.84
CNT-PEI@rGA	364.24	1.75	3.83

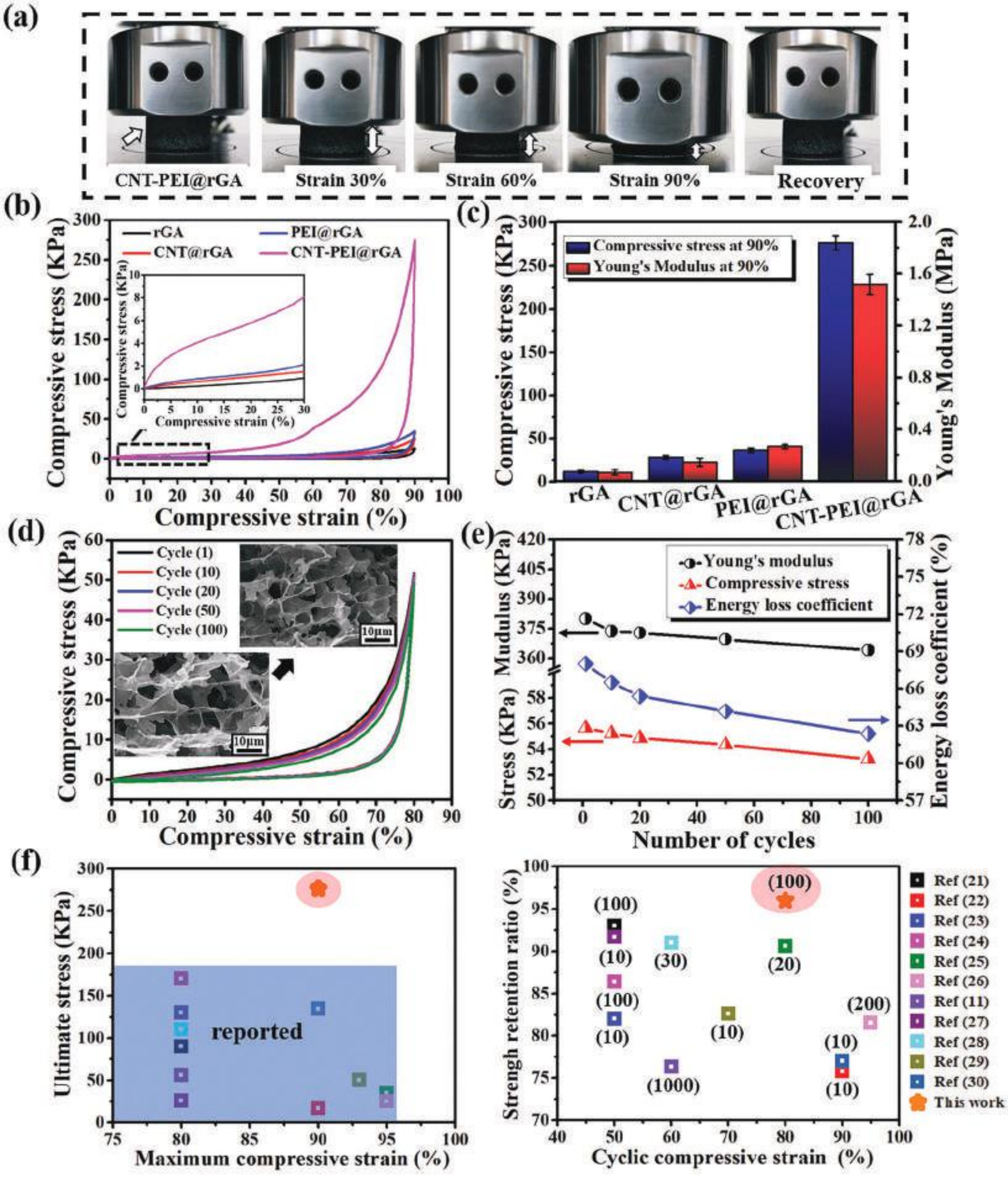

Figure 4. a) Snapshots of compression and recovery of CNT-PEI@rGA. b,c) Stress-strain curves at 90% strain, and corresponding ultimate stress and Young's modulus of rGA, CNT@rGA, PEI@rGA, and CNT-PEI@rGA. d) Stress-strain curves of CNT-PEI@rGA at a set 80% strain for 100 cycles, and SEM images (insets) before and after compression cycles. e) Compressive stress, Young's modulus, and energy loss coefficient of CNT-PEI@rGA for 100 cycles. f) Comparison of mechanical properties of CNT-PEI@rGA with reported elastic graphene aerogels, and numbers in parentheses represent numbers of compressive cycles. The detailed data were listed in Table S2 (Supporting Information).

such as larger ultimate stress, up to 90% maximum compressive strain, and higher strength retention ratio. Based on above analysis, ultralight CNT-PEI@rGA exhibited high strength, super-elasticity, and excellent fatigue-resistance during compression because formation of well-interconnected network skeleton by enhanced crosslinking effect of CNT-PEI avoided the sliding or splitting of rGO sheets along a certain direction when undergoing external force. Meanwhile, entangled CNT-PEI embedded between rGO layers reinforced and supported relatively flexible rGO cell walls to resist external forces.

2.3. Formaldehyde Removal Performance of CNT-PEI@rGA and Its Application for Polyoxymethylene-Based Composites with Low Formaldehyde Emission

The combinations of well-interconnected 3D network, considerable specific surface area, abundant surface amine groups, and excellent mechanical stability yield wide application prospects of as-prepared aerogels in formaldehyde (FA) removal predictably. Based on static adsorption experiment in a sealed chamber (≈10 ppm FA concentration), FA removal rate of

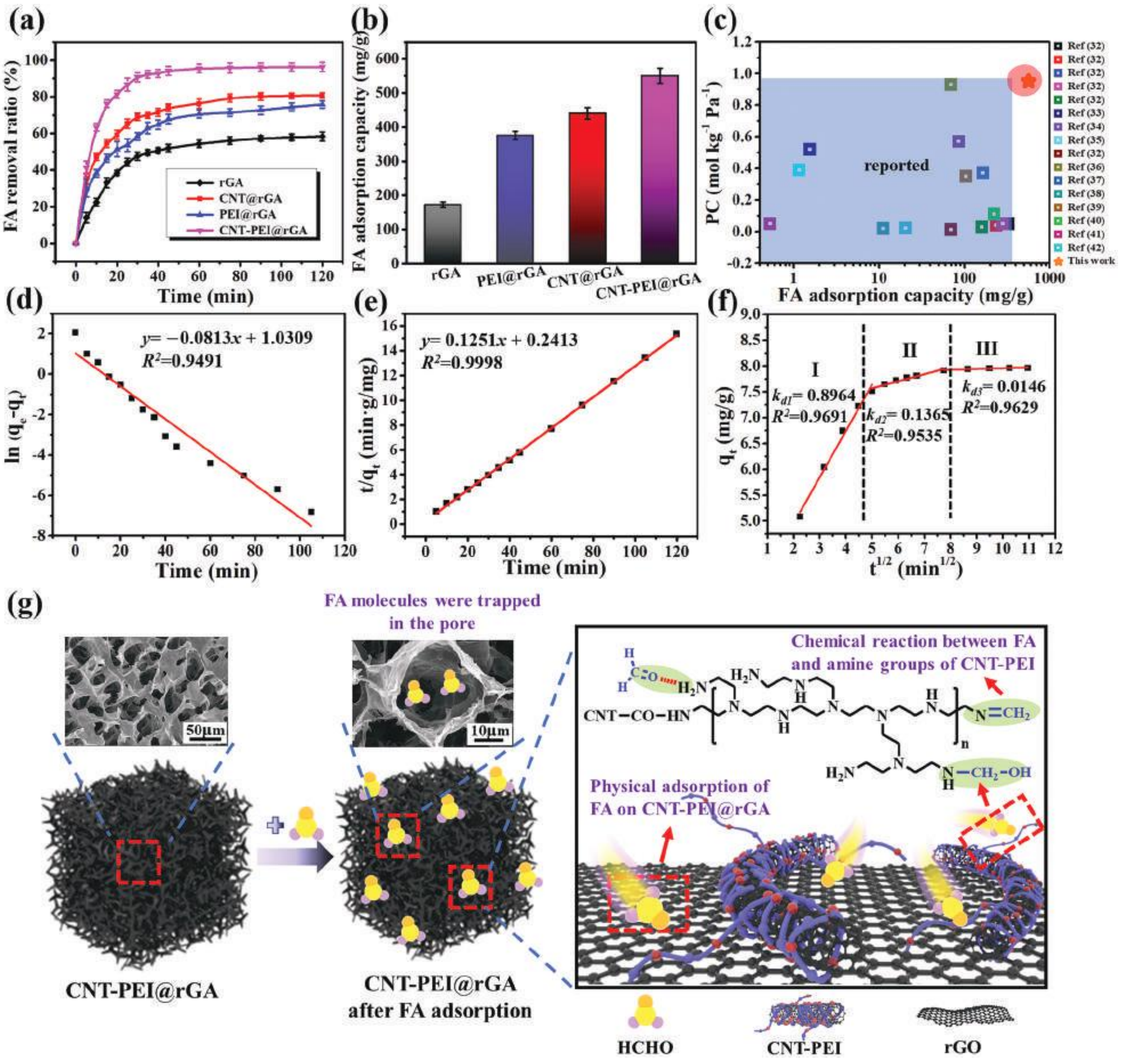

Figure 5. a) FA removal ratio and b) maximum adsorption capacity of rGA, CNT@rGA, PEI@rGA, and CNT-PEI@rGA. c) Comparison of FA adsorption properties of CNT-PEI@rGA with reported adsorbents, and the detailed data were listed in Table S3 (Supporting Information). d,e) Kinetic fitting curves, f) Webber-Morris model of CNT-PEI@rGA, and g) possible FA adsorption mechanism of CNT-PEI@rGA.

aerogel samples varying with time within 120 min was shown in **Figure 5**a. In all cases, the FA removal ratio increased rapidly within initial 30 min, and then gradually levels off to approach the adsorption–desorption equilibrium. By comparison, the order of FA removal ratio measured in the whole process, was CNT-PEI@rGA (96.38%) > CNT@rGA (80.74%) > PEI@rGA (75.83%) > rGA (58.32%), while CNT-PEI@rGA showed maximum removal efficiency and reached the equilibrium ultrafast. It is noteworthy that high-efficient FA removal ratio stayed still stable under multiple compression in Figure S5 (Supporting Information). Furthermore, maximum adsorption capacity was investigated by extending adsorption time (≈48 h) under higher initial FA concentration (≈200 ppm) in Figure 5b. Likewise, maximum adsorption capacity of PEI@rGA and CNT@rGA increased to 376.24 mg g^{-1} and 440.73 mg g^{-1}, respectively, while CNT-PEI@rGA exhibited highest FA adsorption capacity (568.41 mg g^{-1}), ≈3.28 times of rGA (173.32 mg g^{-1}). Besides, the partition coefficient (PC) was used to evaluate FA adsorption performance of different materials at an equivalent level to overcome the limitation based on adsorption capacity concept, derived by dividing the adsorption capacity value with the partial pressure of closed chamber.[31] As shown in Figure 5c and Table S3 (Supporting Information), maximum adsorption capacity and PC value of CNT-PEI@rGA were superior to those of most reported FA adsorbents, e.g., zeolite,[32] activated carbon,[33–35] metal-organic frameworks (MOF),[32,36,37] porous organic polymers[38,39] and other adsorption materials.[40–42] Hence, CNT-PEI@rGA has excellent FA removal properties, including efficient adsorptive activity and high adsorption capacity.

To further explore adsorption mechanism, the adsorption fitting curve of CNT-PEI@rGA within 120 min was shown in Figure 5d–e, using the pseudo-first-order and pseudo-second-order models. The two models[43] were as follows:

$$\text{Pseudo}-\text{first}-\text{ordermodel}: \ln\left(q_e - q_t\right) = \ln q_e - k_1 t \tag{1}$$

$$\text{Pseudo}-\text{second}-\text{ordermodel}: \frac{t}{q_t} = \frac{1}{k_2 q_e^2} + \frac{1}{q_e} t \tag{2}$$

where q_e (mg g^{-1}) and q_t (mg g^{-1}) were the FA adsorption capacity at equilibrium and time t (min), k_1 (min^{-1}) and k_2 (mg g^{-1} min^{-1}) were the pseudo-first-order and pseudo-second-order rate constant, respectively. It was found that correlation coefficient of pseudo-second-order model ($R^2 = 0.9998$) was much higher than that of pseudo-first-order model ($R^2 = 0.9491$), demonstrating that adsorption process of CNT-PEI@rGA indeed involved chemical reactions. Furthermore, Webber-Morris model[44] was used to analyze diffusing process of FA molecules into aerogel in Figure 5f, which was described with Equation (3):

$$\text{Webber}-\text{Morrismodel}: q_t = k_d t^{1/2} + c \tag{3}$$

where q_t (mg g^{-1}) and k_d (mg g^{-1} min$^{-1/2}$) were the FA adsorption capacity at time t (min) and rate constant, respectively. The fitting curve was divided into three parts: fast diffusion stage ($k_{d1} = 0.8964$) ascribed to the effective contact between FA gas and surface pores of CNT-PEI@rGA, rate-limiting stage mediated by chemical reaction ($k_{d1} = 0.1365$), and adsorption equilibrium stage ($k_{d1} = 0.0146$). Moreover, according to XPS analysis of CNT-PEI@rGA before and after FA adsorption in Figure S6 (Supporting Information), the intensity of peaks at 531.55 eV (C–O) in O_{1s} spectra and 398.2 eV (C–N and C=N) in N_{1s} spectra was greatly enhanced, whereas peak intensity at 399.55 eV (amine groups) was weakened for sample after adsorption, further confirming the formation of methylol (–NH–CH$_2$–OH) and imine structures (–C=N–) via the reaction between FA and –NH$_2$. Hence, FA gas removal of CNT-PEI@rGA was a consequence of synergistic chemical-physical adsorption effect as summarized in Figure 5g: owing to introduction of CNT-PEI, well-interconnected 3D network and sufficient interlayer gaps yielded high specific surface area to provide more physical affinity site of FA molecules. Furthermore, some trapped FA molecules reacted with rich amine groups of CNT-PEI through addition chemical reaction.

In addition, CNT-PEI@rGA was ground into powders for subsequent melt processing with POM granules to further expand its application for production of POM-based composites with low FA emission. In **Figure 6**a–b, it was found that CNT-PEI@rGA powders after grinding still retained abundant pores by SEM observation, while its specific surface area was higher than that of GO, CNT-PEI/rGO hybrid, and even CNT-PEI@rGA monoliths. Besides, for POM/0.5 wt.% CNT-PEI@rGA (POM/CGA-0.5), SEM images showed uniform dispersion of CNT-PEI@rGA powders in POM matrix in Figure 6c. FEAs of various POM-based composite samples were investigated in detail. As shown in Figure 6d, compared with POM (FEA: 164 mg kg^{-1}) and POM/0.5 wt.% CNT-PEI/rGO (POM/CGO-0.5) (FEA: 82 mg kg^{-1}), FEA of POM/CGA-0.5 at 60 °C was 65 mg kg^{-1}, decreased by 60.36% and 20.73%, respectively. More intuitively, for POM samples (insets of Figure 6d), the yellow colour of free FA and acetylacetone & ammonium solution was presented, while it became lighter for POM/CGO-0.5. By contrast, very light color was observed for mixed solution of POM/CGA-0.5, indicating that less complexes were produced by reaction between extracted free FA and acetylacetone & ammonium acetate.[45] These results confirmed residual free FA generated from synthesis and processing of POM decreased efficiently. As for FEA at 230 °C, POM/CGA-0.5 also exhibited lowest value (1201 ppm) in Figure 6d, decreased by 63.64% and 19.98% in comparison with POM (3303 ppm) and POM/CGO-0.5 (1501 ppm), respectively, demonstrating effective removal of formaldehyde derived from thermal degradation of POM at high temperature. Similarly, as shown in Figure 6e,f, the FEA at both 60 °C and 230 °C decreased gradually with increasing content of CNT-PEI@rGA powders, while corresponding values of POM/CGA-0.9 were ≈69.63% and 73.96% lower than those of POM, respectively. Therefore, incorporation of CNT-PEI@rGA was conducive to reducing formaldehyde emission of POM significantly.

2.4. Electrical Conductivity and Piezoresistive-Sensing Properties of CNT-PEI@rGA

Figure S7 (Supporting Information) showed elasticity-responsive conductivity of aerogels samples. As shown in Figure S7(a) (Supporting Information), the initial conductivity (5.5 S m^{-1}) of CNT-PEI@rGA was much higher than those of rGA (0.9 S m^{-1}), PEI@rGA (1.6 S m^{-1}), and CNT@rGA (2.6 S m^{-1}), benefited from restored sp^2 regions of rGO due to reduction, and well-interconnected 3D network owing to incorporation of conductive CNT-PEI. Notably, electrical conductivity of CNT-PEI@rGA increased gradually as applied strain increased during the loading process, and it was up to 9.8 S m^{-1} upon 90% strain in Figure S7(b) (Supporting Information). More vividly, the LED bulb was lighted when linked with CNT-PEI@rGA, and it became brighter when it was compressed. These results indicated that mutual contacts of rGO sheets embedded with CNT-PEI constructed more conductive pathways, resulting in corresponding decrease of its electrical resistance under strain stimulation, as depicted in Figure S7(c) (Supporting Information).

Given that it possesses superior mechanical resilience and elasticity-responsive conductivity, CNT-PEI@rGA exhibits an application potential as piezoresistive sensors. Hence, the piezoresistive-sensing properties of CNT-PEI@rGA sensor as assembled schematically in **Figure 7**a were further explored. The current-voltage (I-V) plots of sensor from -1 to 1 V confirmed the linear relationship and steady responses under different compressive strain in Figure S8(a) (Supporting Infor-

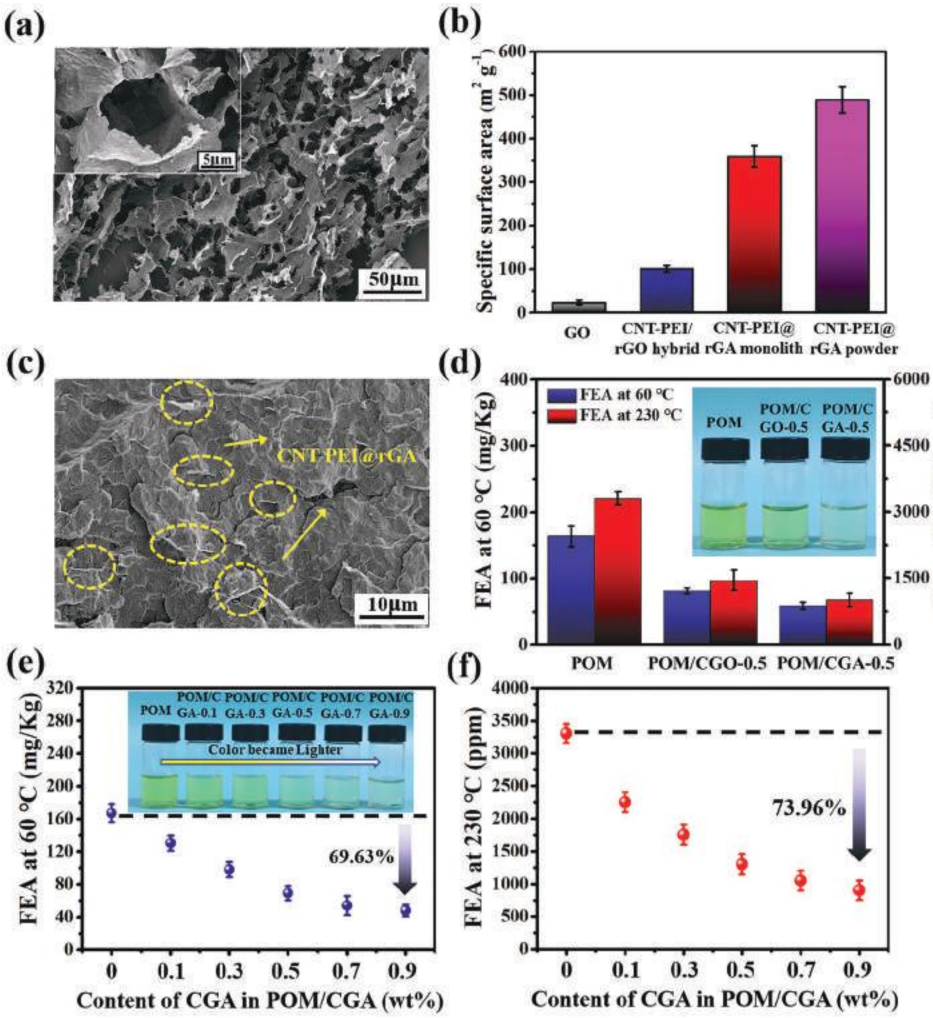

Figure 6. a) SEM images of CNT-PEI@rGA powder after grinding with low and high magnification (inset). b) BET specific surface area of GO, CNT-PEI/rGO hybrid, CNT-PEI@rGA monolith and CNT-PEI@rGA powder. c) SEM images of POM/CGA-0.5. d) FEA of POM, POM/CGO-0.5, and POM/CGA-0.5 and e,f) FEA of POM/CGA with different CNT-PEI@rGA powder content at 60 °C and 230 °C, insets: free formaldehyde and acetylacetone & ammonium solutions.

mation), suggesting good ohmic contact and the decrease of resistance under strain. Besides, the real-time current change response ($\Delta I/I_0$-t curves) at 0–90% strains was shown in Figure 7b. Apparently, a fast and synchronous $\Delta I/I_0$ was exhibited with changing strain during load-unload process, i.e., increasing rapidly under compressing, decreasing immediately upon releasing, and remaining unchanged under a certain strain, which indicated excellent sensing ability to detect a wide range of compressive strain. More importantly, the sensor showed rapid response (0.55s) and recovery time (0.49s) in Figure 7c. Besides, gauge factor (GF)[46] was used to characterize sensitivity of strain sensor, which was calculated with Equation (4):

$$GF = \frac{\Delta I/I_0}{\Delta \varepsilon} = \frac{\Delta I - I_0 \Delta / I_0}{\varepsilon - \varepsilon_0} \quad (4)$$

where I and ε represent the measured current and corresponding applied strain, I_0 and ε_0 were the initial current and strain, respectively. Figure 7d revealed that GF curve was divided into three linear regions: ε = 0–50% (GF = 1.58); ε = 50–70% (GF = 3.85); and ε = 70–90% (GF = 15.92). Obviously, strain sensitivity in large deformation region is superior to that under the initial deformation stage due to high strength and modulus of CNT-PEI@rGA. To further evaluate device stability, the as-fabricated sensor was compressed repeatedly for 10 times at different strains (10-90%), and uniform and stable current signal response over time under all applied strains were observed in Figure 7e. Meanwhile, 1000 cycles of loading–unloading test were performed at a set strain of 30% in Figure 7f. It was found that curves showed very small fluctuations in the output current, and no significant amplitude change was observed at both ends in the magnified insets, demonstrating long-term durability of CNT-PEI@rGA based sensor.

Furthermore, we attached the assembled senor to the muscles or joints of human body to capture real-time physical signal, as shown in Figure 7g–j and Figure S8(b) (Supporting Information), which distinguished clearly motion states by

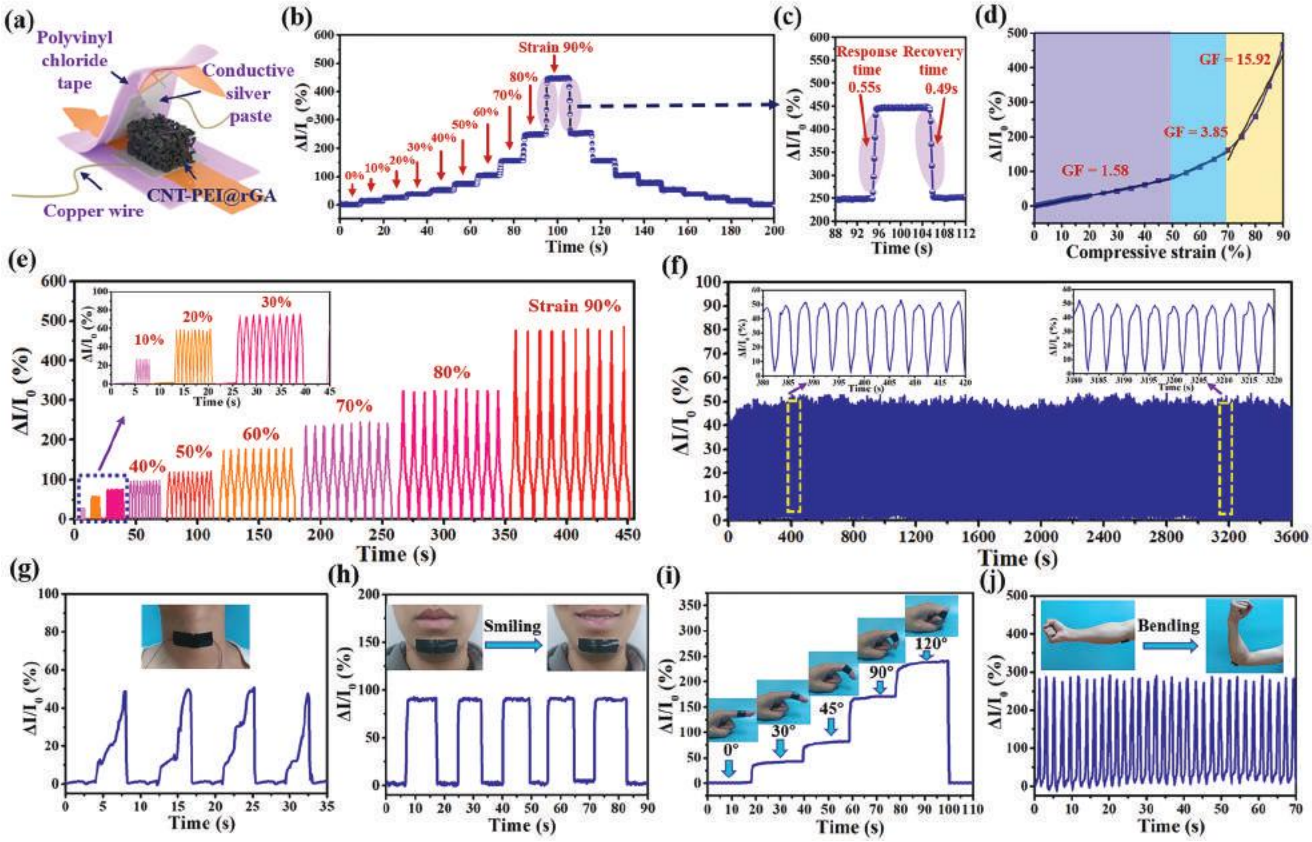

Figure 7. a) Schematic diagram of assembly of CNT-PEI@rGA based sensor. b) Real-time current change of assembled sensor at 0–90% strains. c) Response and recovery time of assembled sensor. d) Plot of $\Delta I/I_0$ versus compressive strain for assembled sensor. e,f) Real-time current change of assembled sensor under 10 times repeated compression at various strains and 1000 compression cycles at a set 30% strain. g–j) Relative current change of assembled sensor monitoring g) swallowing, h) smile, i) forefinger bending, and j) elbow joint bending.

comparing the shape and intensity. Specifically, the device was attached on the throat to monitor swallowing movement (Figure 7g) and below mouth to detect the motion of smile (Figure 7h). It was found that corresponding relative current responses were almost repeatable under the same motion drive. Moreover, the current signal of sensor increased with stepwise increasing forefinger bending angles from 0° to 120° in Figure 7i, while it was stable and repeatable with fast response time in Figure 7j, when senor was adhered to elbow joint subjecting to cyclic bending-straightening motions. Interestingly, when attached to knees, the relative current signals were monitored to behave differently and exhibited periodical response for bending, walking, and running movement, as depicted in Figure S8(b) (Supporting Information). In short, CNT-PEI@rGA-based sensor has the advantages of wide strain detection range, fast response, and good fatigue resistance, which provides promising application prospects as wearable devices for monitoring human activities.

2.5. Thermal Insulation Properties of CNT-PEI@rGA

Benefiting from porous 3D network framework, CNT-PEI@rGA was suitable for thermal insulation materials. As shown in Figure S9 (Supporting Information), CNT-PEI@rGA exhibited excellent thermal stability by TGA analysis, while thermal conductivity of CNT-PEI@rGA was 0.027 W m^{-1} K^{-1}, close to that of air. The thermal conductive behavior of porous materials depended mainly on the thermal conductivity of both gas within pores and solid cell walls. Because the thermal conductivity of gas is much lower than that of solid,[47] the CNT-PEI@rGA sample was filled with abundant air molecules owing to high porosity and ultralow density, which restricted transfer of heat significantly, resulted in an ultralow thermal conductivity and excellent thermal insulation performance.

Furthermore, in **Figure 8**a, a paper crane on asbestos net was heated with a burning alcohol lamp and after ≈30 s, it was already burned with blackened and carbonized bottom. In contrast, when the paper crane was separated from asbestos net by using CNT-PEI@rGA to block heat transfer, no smoke and blackened phenomena were observed in the whole burning process lasting for 60 s. Besides, surface temperature of CNT-PEI@rGA was recorded further in Figure 8b, and the temperature of front side contacting with flame was up to ≈400 °C, while temperature on the back side increased from 46.1 °C to 70.3 °C and 81.5 °C after burning for 30 s and 60 s, respectively, and tended to stabilize at ≈83.4 °C after burning for 120 s. These results confirmed the superior thermal insulation of CNT-PEI@rGA.

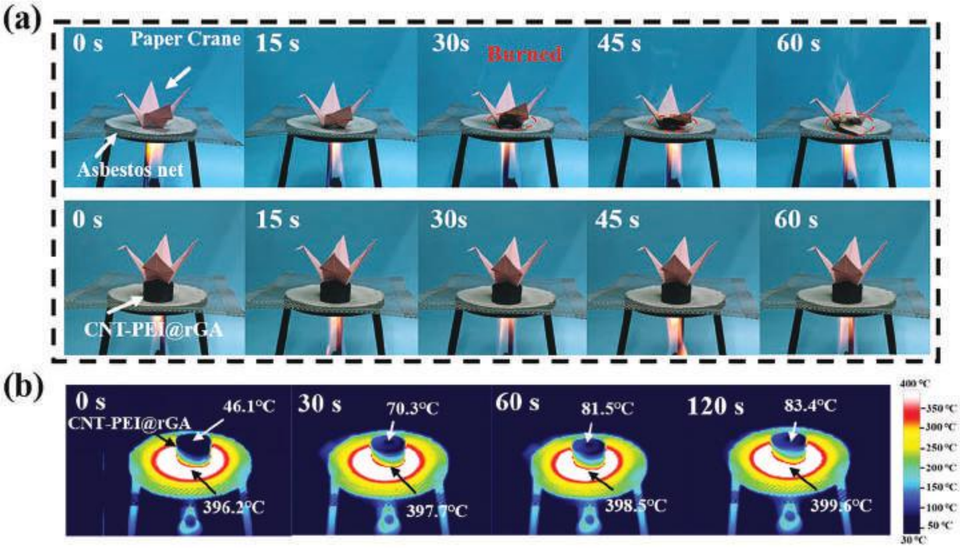

Figure 8. a) Thermal insulation and b) surface temperature of CNT-PEI@rGA heating with an alcohol lamp.

3. Conclusion

In this work, PEI was first grafted chemically onto CNT surface with grafting ratio of 29.34%, and then CNT-PEI@rGA was successfully fabricated via simple hydrothermal assembly, pre-frozen and hydrazine vapor reduction process. The well-interconnected and robust 3D network framework was formed through strong interfacial interaction between GO and CNT-PEI, including covalent bond, hydrogen bonding and π-π interaction. Meanwhile, entangled CNT-PEI was embedded into rGO layers, which led to reinforcement of cell walls to resist external forces and avoided restacking of nanosheets, resulting in much more mesopores and larger specific surface area. Ultralight CNT-PEI@rGA exhibited high ultimate stress of 276.37 kPa, excellent resilience at strain up to 90%, and high strength retention ratio during 100th cyclic compression experiment, which exceeded most reported elastic GAs. Moreover, benefiting from synergistic chemical-physical FA adsorption effect, CNT-PEI@rGA presented high adsorption capacity of 568.41 mg g^{-1}, ≈3.28 times of rGA. POM/ CNT-PEI@rGA composite was then prepared via conventional melt-processing, while FEA of POM/CNT-PEI@rGA-0.9 wt.% was 69.63%/73.96% lower than that of POM at 60 °C/230 °C, respectively. Furthermore, CNT-PEI@rGA showed elasticity-responsive conductivity and remarkable piezoresistive-sensing properties with fast response, a wide strain detection range and long-term durability. Besides, it also exhibited excellent thermal stability and thermal insulation properties. This work provided new strategy for multifunctional GA construction in fields of environmental remediation, smart electronic devices, heat insulating materials, etc.

4. Experimental Section

Materials: Graphene oxide (GO) and carboxyl-functionalized multi-walled carbon nanotubes (CNT-COOH, Purity ≥ 98%) powders were supplied by Chengdu Organic Chemicals Co. Ltd. (China). Polyethyleneimine (PEI, M$_W$ = 10000) was purchased from Huaxia Chemical Reagent Co., Ltd. (China). Thionyl chloride (SOCl$_2$), hydrazine hydrate, N, N-Dimethylformamide (DMF) and triethylamine were all commercial grade products from Kelong Chemical Reagent Factory (China).

Preparation of Materials—Preparation of CNT-PEI@rGA: The CNT-PEI hybrid was prepared as follows[48]: 1.0 g CNT-COOH was dispersed in solution of 250 mL SOCl$_2$ and 5 mL DMF with sonication for 30 min. The mixture was refluxed for 24 h at 70 °C, and unreacted SOCl$_2$ was removed by distillation. Acyl chloride-functionalized carbon nanotubes (CNT-COCl) was then obtained and added to solution of 100 mL DMF and 1 mL triethylamine together with 1.0 g PEI, stirring at 50 °C for 48 h. The products were centrifuged and washed with DMF/water, and dried at 80 °C for 12 h.

CNT-PEI@rGA was synthesized via a simple hydrothermal method, pre-frozen and hydrazine vapor reduction process. GO and CNT-PEI were uniformly dispersed in deionized water at a constant mass ratio of 2:1 by probe sonication for 30 min, with GO concentration of 4 mg mL^{-1}. Next, the mixture was transferred to a Teflon-lined stainless autoclave (25 mL), and hydrothermally treated at 110 °C for 12 h. The obtained hydrogel was dialyzed by deionized water/ethanol solution for 48 h. Afterward, it was fast pre-frozen in liquid nitrogen and freeze-dried at -50 °C for 72 h to obtain composite aerogel. Finally, the aerogel was chemically reduced by hydrazine vapor at 90 °C for 12 h, followed by vacuum-drying at 160 °C for 12 h. For simplicity, the resultant product was denoted as CNT-PEI@rGA.

For comparison, rGO aerogel (in absence of CNT-COOH and PEI), CNT-COOH@rGO aerogel (only with addition of CNT-COOH) and PEI@rGO aerogel (only with adding PEI) were prepared via the same process, denoted as rGA, CNT@rGA, and PEI@rGA, respectively. Note that addition of CNT-COOH or PEI was the same content with CNT-PEI@rGA samples. For comparison of FEA, preparation of CNT-PEI/rGO hybrid was shown in Section S1 (Supporting Information).

Preparation of Materials—Preparation of POM/CNT-PEI@rGA Composite: POM/CNT-PEI@rGA composite was manufactured by conventional melt processing. Specifically, CNT-PEI@rGA was ground into aerogel powder, and then it was processed with POM granules, as well as 0.3 wt.% Irganox245 by using Rheocord System 40 torque rheometer from German HAKKE company at rotational speed of 60 rpm for 5 min at 185 °C. A series of composites were obtained and labelled as POM/CGA-0.1, POM/CGA-0.3, POM/CGA-0.5, POM/CGA-0.7, POM/CGA-0.9, respectively, based on content of CNT-PEI@rGA powder of 0.1wt%, 0.3wt%, 0.5wt%, 0.7wt%, 0.9wt%. For comparison, POM/0.5 wt.% CNT-PEI/rGO was prepared by same method, denoted as POM/CGO-0.5.

Measurements: The structure and element composition of aerogel samples were characterized with Fourier-transform infrared spectrometer (FT-IR) (Nicolet-560, USA), Raman microscope (RENISHAW Invia, UK) and X-ray photoelectron spectroscopy (XPS) (XSAM 800, KRATOS Co., UK). X-ray diffraction (XRD) was performed on a diffractometer (Rigaku D/max III B, Japan) with Cu K_α radiation (λ = 0.154 m) and interlayer spacing (d-spacing) was calculated with Bragg equation. Thermogravimetric analysis (TGA) was conducted with analyzer (TA 2950, USA.) at 10 °C min^{-1} heating rate in nitrogen. Scanning electron microscopy (SEM) (JEOL JSM-5900LV, Japan) equipped with Energy-Dispersive X-ray Spectroscopy (EDS) were carried out to observe morphologies and element distribution of aerogel samples, which were brittle fractured and coated with gold. Transmission electron microscopy (TEM) (JEOL JEM 100CX II, Japan) images and electron diffraction (SAED) patterns of selected area were acquired at 200 kV, and aerogel dispersion were drop-casting onto the copper grid. Nitrogen sorption isotherms were measured with analyzer (Autosorb-IQ2, USA) at 77 K and evaluated using Brunauer-Emmett-Teller (BET) and Barrett–Joyner–Halenda (BJH) methods. The densities of cylindrical aerogel samples were calculated with Equation (5):

$$\rho = \frac{m}{\pi r^2 \times h} \tag{5}$$

where m is weight measured by analytical balance, r and h are radius and height measured with vernier caliper.

Note that important performance characterizations were shown in Section S1 (Supporting Information).

Supporting Information

Supporting Information is available from the Wiley Online Library or from the author.

Acknowledgements

This work was supported by National Natural Science Foundation of China (No.51933007), Natural Science Foundation of Sichuan Province (No.2022NSFSC0355), Project of Engineering Characteristic Team of Sichuan University, and Fundamental Research Funds for the Central Universities.

Conflict of Interest

The authors declare no conflict of interest.

Data Availability Statement

The data that support the findings of this study are available from the corresponding author upon reasonable request.

Keywords

enhancing mechanical strength and resilience, formaldehyde removal, graphene aerogel (GA), multifunctional applications, well-interconnected 3D network structures

Received: January 9, 2023
Revised: February 9, 2023
Published online:

[1] J. Mao, J. Iocozzia, J. Huang, K. Meng, Y. Lai, Z. Lin, *Energy Environ. Sci.* **2018**, *11*, 772.
[2] T. Yan, T. Li, J. Xu, J. Chao, R. Wang, Y. I. Aristov, L. G. Gordeeva, P. Dutta, S. S. Murthy, *ACS Energy Lett.* **2021**, *6*, 1795.
[3] X. Cao, J. Zhang, S. Chen, R. J. Varley, K. Pan, *Adv. Funct. Mater.* **2020**, *30*, 2003618.
[4] J. Xiao, Y. Tan, Y. Song, Q. Zheng, *J. Mater. Chem. A* **2018**, *6*, 9074.
[5] B. Liu, X. Ren, L. Chen, X. Ma, Q. Chen, Q. Sun, L. Zhang, P. Si, L. Ci, *J. Hazard. Mater.* **2019**, *373*, 705.
[6] J. Qu, D. Chen, N. Li, Q. Xu, H. Li, J. He, J. Lu, *Small* **2018**, *14*, 1800343.
[7] J. D. Afroze, M. J. Abden, Z. Yuan, C. Wang, L. Wei, Y. Chen, L. Tong, *Carbon* **2020**, *162*, 365.
[8] P. Song, B. Liu, C. Liang, K. Ruan, H. Qiu, Z. Ma, Y. Guo, J. Gu, *Nano-Micro Lett.* **2021**, *13*, 91.
[9] X. He, Q. Liu, W. Zhong, J. Chen, D. Sun, H. Jiang, K. Liu, W. Wang, Y. Wang, Z. Lu, M. Li, X. Liu, X. Wang, G. Sun, D. Wang, *ACS Appl. Mater. Interfaces* **2019**, *11*, 19350.
[10] S. Kang, S. Qiao, Y. Cao, Z. Hu, J. Yu, Y. Wang, *Chem. Eng. J.* **2022**, *433*, 133619.
[11] P. Lv, X.-W. Tan, K.-H. Yu, R.-L. Zheng, J.-J. Zheng, W. Wei, *Carbon* **2016**, *99*, 222.
[12] Y. Qin, Y. Zhang, N. Qi, Q. Wang, X. Zhang, Y. Li, *ACS Appl. Mater. Interfaces* **2019**, *11*, 10409.
[13] J. D. Afroze, L. Tong, M. J. Abden, Z. Yuan, Y. Chen, *Carbon* **2021**, *175*, 312.
[14] L. Liu, J. Liu, Y. Zeng, S. J. Tan, D. D. Do, D. Nicholson, *Chem. Eng. J.* **2019**, *370*, 866.
[15] T. Alizadeh, L. H. Soltani, *J. Hazard. Mater.* **2013**, *248*, 401.
[16] J. Ma, Y. Sun, J. Yang, Z. Lin, Q. Huang, T. Ou, F. Yu, *Aerosol Air Qual. Res.* **2017**, *17*, 913.
[17] L. Wu, L. Zhang, T. Meng, F. Yu, J. Chen, J. Ma, *Aerosol Air Qual. Res.* **2015**, *15*, 1028.
[18] W. Zhang, T. Huang, Y. Ren, Y. Wang, R. Yu, J. Wang, Q. Tu, *Int. J. Biol. Macromol.* **2021**, *193*, 2243.
[19] S. Stankovich, D. A. Dikin, R. D. Piner, K. A. Kohlhaas, A. Kleinhammes, Y. Jia, Y. Wu, S. T. Nguyen, R. S. Ruoff, *Carbon* **2007**, *45*, 1558.
[20] H. Sun, Z. Xu, C. Gao, *Adv. Mater.* **2013**, *25*, 2554.
[21] X. Wang, L.-L. Lu, Z.-L. Yu, X.-W. Xu, Y.-R. Zheng, S.-H. Yu, *Angew. Chem., Int. Ed.* **2015**, *54*, 2397.
[22] Z. Wang, X. Shen, M. A. Garakani, X. Lin, Y. Wu, X. Liu, X. Sun, J.-K. Kim, *ACS Appl. Mater. Interfaces* **2015**, *7*, 5538.
[23] N. Ni, S. Barg, E. Garcia-Tunon, F. M. Perez, M. Miranda, C. Lu, C. Mattevi, E. Saiz, *Sci. Rep.* **2015**, *5*, 13712.
[24] L. Wang, J. Wang, L. Wu, X. Wang, *Composites, Part A* **2021**, *140*, 106195.
[25] Q. Zhang, X. Xu, H. Li, G. Xiong, H. Hu, T. S. Fisher, *Carbon* **2015**, *93*, 659.
[26] X. Peng, K. Wu, Y. Hu, H. Zhuo, Z. Chen, S. Jing, Q. Liu, C. Liu, L. Zhong, *J. Mater. Chem. A* **2018**, *6*, 23550.
[27] J. Li, W. Li, W. Huang, G. Zhang, R. Sun, C.-P. Wong, *J. Mater. Chem. C* **2017**, *5*, 2723.
[28] Y. Liu, Q. Shi, C. Hou, Q. Zhang, Y. Li, H. Wang, *Carbon* **2017**, *125*, 352.
[29] H. Yang, T. Zhang, M. Jiang, Y. Duan, J. Zhang, *J. Mater. Chem. A* **2015**, *3*, 19268.
[30] M. Yang, N. Zhao, Y. Cui, W. Gao, Q. Zhao, C. Gao, H. Bai, T. Xie, *ACS Nano* **2017**, *11*, 6817.
[31] C.-J. Na, M.-J. Yoo, D. C. W. Tsang, H. W. Kim, K.-H. Kim, *J. Hazard. Mater.* **2019**, *366*, 452.
[32] J.-P. Bellat, I. Bezverkhyy, G. Weber, S. Royer, R. Averlant, J.-M. Giraudon, J.-F. Lamonier, *J. Hazard. Mater.* **2015**, *300*, 711.
[33] G. de Falco, M. Barczak, F. Montagnaro, T. J. Bandosz, *ACS Appl. Mater. Interfaces* **2018**, *10*, 8066.

[34] G. B. Baur, J. Spring, L. Kiwi-Minsker, *Adsorption* **2018**, *24*, 725.
[35] K. Vikrant, D.-H. Lim, S. A. Younis, K.-H. Kim, *Sci. Total Environ.* **2020**, *743*, 140761.
[36] K. Vikrant, M. Cho, A. Khan, K.-H. Kim, W.-S. Ahn, E. E. Kwon, *Environ. Res.* **2019**, *178*, 108672.
[37] Z. Wang, W. Wang, D. Jiang, L. Zhang, Y. Zheng, *Dalton Trans.* **2016**, *45*, 11306.
[38] L. Pan, Q. Chen, J.-H. Zhu, J.-G. Yu, Y.-J. He, B.-H. Han, *Polym. Chem.* **2015**, *6*, 2478.
[39] K. Vikrant, Y. Qu, K.-H. Kim, D. W. Boukhvalov, W.-S. Ahn, *Environ. Sci.: Nano* **2020**, *7*, 3447.
[40] Y. Liao, X. Pan, *Environ. Sci.: Nano* **2021**, *8*, 1283.
[41] W. Zhang, L. Chen, L. Xu, H. Dong, H. Hu, Y. Xiao, M. Zheng, Y. Liu, Y. Liang, *J. Colloid Interface Sci.* **2019**, *537*, 562.
[42] Y. Le, D. Guo, B. Cheng, J. Yu, *Appl. Surf. Sci.* **2013**, *274*, 110.
[43] J. Zhu, J. Chen, P. Zhuang, Y. Zhang, Y. Wang, H. Tan, J. Feng, W. Yan, *Atmos. Pollut. Res.* **2021**, *12*, 1.
[44] M. A. Albakri, M. M. Abdelnaby, T. A. Saleh, O. C. S. Al Hamouz, *Chem. Eng. J.* **2018**, *333*, 76.
[45] Y. Kawakami, Y. Y. Maruo, T. Nakagawa, H. Saito, *Measurement* **2015**, *62*, 41.
[46] P. Liu, X. Li, X. Chang, P. Min, C. Shu, Y. Li, Y. Kang, Z.-Z. Yu, *Carbon* **2021**, *178*, 301.
[47] H. Yu, H. Zhang, J. Zhao, J. Liu, X. Xia, X. Wu, *Front. Phys.* **2022**, *17*, 23202.
[48] W. Wang, Z. Zhang, X. Zhao, L. Ye, *Polym. Degrad. Stab.* **2022**, *198*, 109876.